

Synergy of nuclear and electronic energy losses in ion-irradiation processes: The case of vitreous silicon dioxide

Marcel Toulemonde,¹ William J. Weber,^{2,3} Guosheng Li,⁴ Vaithiyalingam Shutthanandan,⁴ Patrick Kluth,⁵ Tengfei Yang,⁶ Yuguang Wang,⁶ and Yanwen Zhang^{3,2,*}

¹*CIMAP-CEA-CNRS-ENSICAEN-University of CAEN, F-14070 Caen Cedex 5, France*

²*Department of Materials Science and Engineering, University of Tennessee, Knoxville, Tennessee 37996, USA*

³*Materials Science and Technology Division, Oak Ridge National Laboratory, Oak Ridge, Tennessee 37831, USA*

⁴*Pacific Northwest National Laboratory, Richland, Washington 99352, USA*

⁵*Australian National University, Canberra ACT 0200, Australia*

⁶*Peking University, Beijing, China*

(Received 22 October 2010; published 16 February 2011)

Structural modification of vitreous SiO₂ by Au ion irradiation is investigated over an energy regime (~ 0.3 –15 MeV) in which the decrease of the nuclear energy loss with increasing energy is compensated by the increase of the electronic energy loss, leading to a nearly constant total energy loss of ~ 4 keV/nm. The radii of damaged zones resulting from the ion impact, deduced from changes in infrared bands as a function of ion fluence, decrease from 4.9 nm at 0.3 MeV to 2.5 and 2.6 nm at 9.8 and 14.8 MeV, respectively. Based on previous data where vitreous SiO₂ was irradiated with much higher energy Au ions, the damage zone radius increases from 2.4 nm at 22.7 MeV to 5.4 nm at 168 MeV, and a U-shaped dependence on energy is observed in the energy region from 0.3 to 168 MeV. The current results demonstrate that large damage radii at low and high ion energy can be explained by the elastic or inelastic thermal spike model, respectively. In the transition regime where both nuclear and electronic energy loss are significant, a unified thermal spike model consisting of a coherent synergy of the elastic collision spike model with the inelastic thermal spike model is suggested to interpret and describe the radius evolution from the nuclear to the electronic energy regime.

DOI: [10.1103/PhysRevB.83.054106](https://doi.org/10.1103/PhysRevB.83.054106)

PACS number(s): 61.80.Jh, 61.05.cf, 61.43.Bn, 61.43.Fs

I. INTRODUCTION

Vitreous SiO₂ is a material widely used in electronic devices or waveguides for light transportation. This material is often subjected to ion irradiation in industrial fabrication processes and in space applications by cosmic rays. Moreover, vitreous SiO₂, with additional glass formers to reduce the melting temperature, is the basis for borosilicate glass used for nuclear waste immobilization, which is exposed to extreme radiation doses from α decay of the actinides and β decay of the fission products.^{1,2} Structural modification through atomic displacements and electronic energy deposition may compromise the physical and chemical durability of such materials. Previous work on ion-irradiation-induced property changes or structural modifications in vitreous SiO₂ have focused on swift heavy ions.^{3–7} Recently, the prospects of etching ion tracks produced by low- and medium-energy ion beams have attracted much attention,^{8,9} where the energy regime is suitable for nanostructuring thin films in microelectronic devices or waveguides, particularly in systems like SiO₂/Si.¹⁰ In the energy regime from approximately 1.5 to 75 keV/amu (or equivalently 0.3 to 15 MeV¹⁹⁷Au ions), the role of the nuclear energy deposition and the existence of synergistic effects between nuclear (dE/dx_{nucl}) and electronic (dE/dx_{ele}) energy losses on the structural modification remains unclear. In this work, vitreous SiO₂ films are investigated as a model system to study the behavior of an insulating glass under ion irradiation in an energy regime where both the nuclear^{11–15} and electronic energy losses^{3–7} are significant.

In the electronic energy loss regime, structural modifications in vitreous SiO₂, such as compaction of the material

followed by an anisotropic growth,^{4,16–20} are detectable only above a certain threshold value of electronic energy loss. Depending on the ion velocity,²¹ different $S_e(-dE/dx_{\text{ele}})$ thresholds exist, varying from 0.4 keV/nm for energies at ~ 0.01 MeV/amu (Ref. 20) to 2.0 keV/nm for energies at ~ 5.0 MeV/amu.⁴ Compaction of the glass matrix is attributed to the reordering of the Si–O tetrahedral network associated with a decrease of the O–Si–O bond-angle. This compaction can be detected using infrared spectroscopy to follow the evolution of the TO3 absorption band, an asymmetric vibrational stretching mode, as a function of ion fluence. The change of the TO3 band versus ion fluence^{5,6} enables a determination of the track damage radius by fitting to a Poisson law. Since the structure of individual ion tracks is difficult to observe directly in amorphous materials, it is only recently that track radii larger than 2.4 nm have been deduced from small-angle x-ray scattering (SAXS) measurements,³ where S_e is larger than 4 keV/nm for Au ions with energies higher than 22 MeV. In previous works, vitreous SiO₂ has been irradiated with Au ions in an energy range where the electronic energy loss increases with ion energy [between 2 and 120 MeV,^{3,9,19,20} corresponding to S_e ranging between 1.7 and 12 keV/nm according to the Stopping and Range of Ions in Matter (SRIM) calculation].²² In this range, an increase in the rate of anisotropic growth is observed with increasing electronic energy loss.¹⁹ Furthermore, the chemical etching efficiency^{9,23,24} first increases with the electronic energy loss and then saturates for S_e values larger than ~ 4 keV/nm. None of these previous experiments has provided evidence that nuclear energy loss of Au ions contributes to the structural modification of vitreous SiO₂.

TABLE I. Ion-irradiation parameters and damage cross sections (σ_{exp}) determined from infrared spectroscopy for the two bands (1044 and 1078 cm^{-1}). E_{irr} is the ion energy from the accelerator, and E_{av} is the average ion energy in the SiO_2 film. The film is 104 nm thick with a density of 2.2 g cm^{-3} . dE/dx_{ele} and dE/dx_{nuc} are the averaged electronic and nuclear energy loss, respectively, predicted by SRIM within the SiO_2 film,²² and σ_{TRIM} is the TRIM-predicted damage cross section.^{22,40} The total energy loss, dE/dx_{total} , is the sum of dE/dx_{ele} and dE/dx_{nuc} .

Ion	E_{irr} (MeV)	E_{av} (MeV)	dE/dx_{ele} (keV/nm)	dE/dx_{nuc} (keV/nm)	dE/dx_{total} (keV/nm)	σ_{TRIM} (10^{-13} cm^2)	σ_{exp} (1044) (10^{-13} cm^2)	σ_{exp} (1078) (10^{-13} cm^2)	Mean σ_{exp} (10^{-13} cm^2)
Au	0.5	0.3	0.71	3.2	3.9	0.04	8.2	6.6	7.4 ± 1.1
Au	0.8	0.6	1.11	3.1	4.2	0.035	7.2	6.4	6.8 ± 1.0
Au	1.5	1.3	1.40	2.8	4.2	0.03	5.3	4.5	4.9 ± 0.7
Au	2.5	2.3	1.70	2.3	4.0	0.022	3.0	2.5	2.8 ± 0.4
Au	5.0	4.8	2.15	1.8	4.0	0.017	3.4	2.1	2.8 ± 0.7
Au	10	9.8	2.57	1.2	3.8	0.011	2.3	1.5	1.9 ± 0.4
Au	15	14.8	2.95	0.92	3.9	0.008	2.5	1.7	2.1 ± 0.4
Ni	11.6	11.4	4.2	0.08	4.3	0.0011	3.2	2.1	2.7 ± 0.6
Si	5.6	5.5	2.8	0.02	2.8	0.00036	1.8	1.0	1.4 ± 0.4
O	3.2	3.1	1.8	0.008	1.8	0.00013	0.45	0.31	0.38 ± 0.07

We present a systematic study on structural modification of vitreous SiO_2 under Au irradiation at energies ranging from 0.3 to 15 MeV that cover the transition from the nuclear energy loss dominant regime to the nearly pure electronic energy loss regime. It should be pointed out that, in the energy regime between 0.3 and 15 MeV for Au ions, the total energy loss, dE/dx_{total} , is approximately constant, as shown in Table I, since a decrease in nuclear energy loss is compensated by an increase in electronic energy loss. To evaluate the effects of electronic energy loss at low ion velocity, the vitreous SiO_2 was also irradiated by ^{16}O , ^{28}Si , and ^{58}Ni at an energy of 0.2 MeV/amu, where the electronic energy loss is at least 98% of the total energy loss (Table I). In this study, the irradiation-induced structural change in vitreous SiO_2 was characterized by the evolution of the TO3 band using infrared spectroscopy.^{5,6,13,14}

Until now, ion track formation, in either insulators^{3,26} or metallic materials,²⁷ has been described as a consequence of pure electronic stopping using the inelastic thermal spike formalism (i-TS) where nuclear collisions are neglected. In this i-TS model, the energy deposited to the electrons is transferred to the lattice atoms via electron-electron and electron-phonon interactions. Using the i-TS model, it is possible to describe the different track radii resulting from the same electronic energy loss observed either at high energy ($\sim 5.3 \text{ MeV/amu}$)⁶ or at low energy ($\sim 0.45 \text{ MeV/amu}$)²⁸ when irradiated with low-Z ions. For the same electronic energy loss, the energy deposited to the electrons with lower ion velocity²⁹ leads to a more efficient energy transfer to the lattice atoms and consequently to a larger track radius. This phenomenon is called the velocity effect, where the incident ion velocity is taken into account. Extrapolation of this model fails to describe the present results for Au irradiations at energies less than 10 MeV.³ In the present work, a unified thermal spike model containing both the inelastic thermal spike model and the elastic collision spike model^{30,31} is presented to describe ion track formation in an energy regime where electronic and nuclear energy loss are both significant. The results demonstrate that the large structural modifications observed in the nuclear energy loss regime can be described by the modified elastic collision spike model,³¹ and a synergistic effect of nuclear and electronic

energy loss exists in the energy range from ~ 2 to 15 MeV for Au ions where the unified thermal spike model should be applied.

II. EXPERIMENTAL DESCRIPTION AND DATA ANALYSIS

A. Irradiation conditions

Amorphous SiO_2 films of $\sim 104 \text{ nm}$ thickness (mass density of 2.2 g cm^{-3}) were thermally grown on both sides of 2-in.-diam Si (100) wafers. The thin SiO_2 films were used so that the majority of the Au ions fully penetrate the SiO_2 film to minimize the compositional changes. Moreover, both the nuclear and electronic energy loss can be treated as a constant value over the thickness of the film; therefore, averaged stopping values can be used for data analysis and model fitting. The wafers were cut into small samples of $\sim 0.5 \times 0.5 \text{ cm}^2$. The samples were irradiated with Au ions having incident charge states between 1+ and 5+ at 0.5, 0.8, 1.5, 2.5, 5, 10, and 15 MeV, leading to average ion energy values of 0.3, 0.6, 1.3, 2.3, 4.8, 9.8, and 14.8 MeV in passing through the SiO_2 films, as given in Table I. For the light ions, the average beam energies in the film were 3.1, 5.5, and 11.4 MeV for O^{1+} , Si^{2+} , and Ni^{4+} , respectively (Table I). At these energies, the equilibrium charge state of the ions is reached within a depth of less than 5 nm from the surface,³² and it does not influence the determination of the mean electronic energy loss in the sample. The flux varied between 1×10^{10} and $6 \times 10^{10} \text{ ions cm}^{-2} \text{ s}^{-1}$, depending on the intended fluence, which ranged from 1.0×10^{11} to $3 \times 10^{14} \text{ ions cm}^{-2}$.

B. Analysis of the infrared bands: Intensity determination

The ion-irradiation-induced modifications in the SiO_2 films were studied by infrared spectroscopy (Bruker Vertex 70). The results from samples irradiated at 9.8 MeV Au ions are shown in Fig. 1 to demonstrate the evolution of the spectra as a function of irradiation fluence. The infrared spectra are composed of peaks corresponding to the TO3 absorption band over wavelengths ranging from 1000 to 1120 cm^{-1} and to a band corresponding to the LO4-TO4 pair at 1165 and 1200 cm^{-1} . The spectra were recorded at a scanning resolution of 2 cm^{-1}

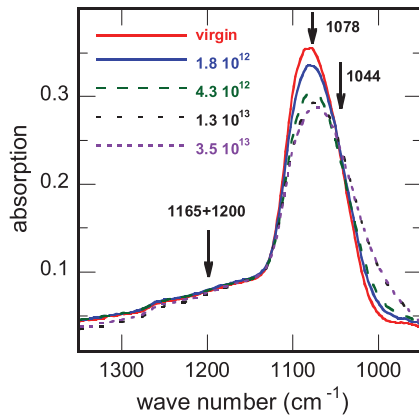


FIG. 1. (Color online) Infrared spectra of 9.8 MeV Au irradiating vitreous SiO₂ in the 950–1350-cm⁻¹ range for different fluences quoted in the figure.

with 64 scans. As shown in Fig. 1, a decrease of the 1078-cm⁻¹ TO3 band is observed with the appearance of a peak at a wavelength of 1044 cm⁻¹. There is no significant change of the intensity of the pair LO4-TO4 band. The spectrum analysis is exemplified in Fig. 2 using the spectra of the virgin sample and samples irradiated at 9.8 MeV to ion fluences of 1.8×10^{12} and 3.0×10^{13} cm⁻². The full width at half maximum (FWHM) of the 1078 and 1197 cm⁻¹ bands has been determined from a Gaussian fit of the nonirradiated sample, yielding 70 and 140 cm⁻¹, respectively, as shown in Fig. 2(a). The width for the 1078 cm⁻¹ band is in good agreement with the results determined previously by Mazzoldi *et al.*¹³ and Busch *et al.*⁵ for dominant nuclear and electronic energy loss, respectively. Due to the existence of the 104 nm vitreous SiO₂ film on the back side of the Si sample, it was not possible to fit independently the position and FWHM of the band at 1044 cm⁻¹. However, by mechanical removal of the SiO₂ on the back side of the sample irradiated at high fluence, the FWHM of the 1044 cm⁻¹ band was determined to be 110 cm⁻¹, in agreement with previous experimental results.^{5,13} The general quality of the spectra and fits are illustrated in Fig. 2, which represents the data analysis procedures for the other

irradiated samples. Keeping the FWHM of each peak constant, the position and the areas of 1078 and 1044 cm⁻¹ bands were deduced by normalized Gaussian fitting for each fluence. From the fit, the position of the peak varies only by 3 cm⁻¹. For the virgin spectrum, the fit was better when a small contribution of the peak at 1044 cm⁻¹ was included.

C. Cross section of structural transformation and radius determination

The decrease of the peak area for the 1078 cm⁻¹ band and the increase of the peak area for the 1044 cm⁻¹ band are shown in Fig. 3 as a function of ion fluence for irradiation with 9.8 MeV Au ions. Under high fluence irradiation, a saturation level is reached for both the increase of the 1044 cm⁻¹ peak and the reduction of the 1078 cm⁻¹ peak. Also included is the sum of the two bands, which remains constant, suggesting that the decrease of the 1078 cm⁻¹ band is compensated by the increase of the 1044 cm⁻¹ band. A similar evolution of both bands was observed for all the irradiations. At large fluences, the minimum level of the peak area for the 1078 cm⁻¹ band results from infrared (IR) absorption in the unirradiated vitreous SiO₂ on the back side of the sample.

The evolution of the peak area as a function of fluence (Φt), as shown by the data points in Figs. 3 and 4, is fitted using a Poisson law,³³ which defines the probability for an incident ion to impact the virgin part of the sample with a cross section σ . For the 1078 cm⁻¹ peak, $Z(\Phi t) = [Z_0(\Phi t = 0) - Z_{\min}(\Phi t = \infty)] * e^{-(\sigma_{\text{exp}} * \Phi t)} + Z_{\min}(\Phi t = \infty)$ is used, while for the 1044 cm⁻¹ peak, the complementary part $Y(\Phi t) = [Y_{\max}(\Phi t = \infty) - Y_0(\Phi t = 0)] * (1 - e^{-(\sigma_{\text{exp}} * \Phi t)}) + Y_0(\Phi t = 0)$ is used. The corresponding results are plotted as solid and dotted lines for the 1044 and 1078 cm⁻¹ peaks, respectively, in Figs. 3 and 4 for different irradiations. The damage cross section (σ_{exp}) for each irradiation is obtained from the fit parameter and is given in Table I for Au, Ni, Si, and O irradiations.

Assuming a cylindrical geometry for the ion track, the radii are derived from the relation $R_{\text{exp}} = (\sigma_{\text{exp}}/\pi)^{1/2}$ and summarized in Tables II and III. The track radii for the O, Si, and Ni irradiations are shown in Fig. 5 as a function

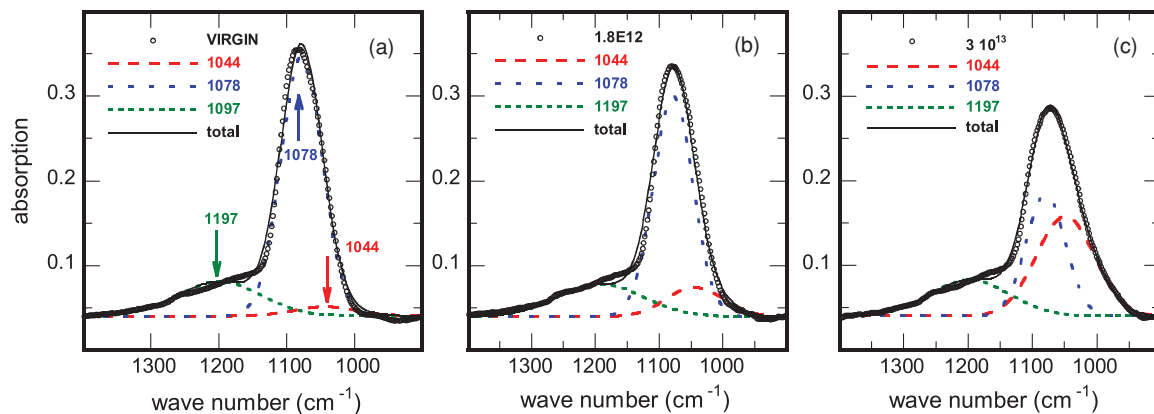


FIG. 2. (Color online) Infrared spectra from the vitreous SiO₂ samples (a) unirradiated and (b) and (c) irradiated with 9.8 MeV Au ions to fluences of 1.8×10^{12} and 3.0×10^{13} ions/cm², respectively. The individual contributions obtained from the fits corresponding to the 1044 (long dashed line), 1078 (short dashed line), and 1197 (dotted line) cm⁻¹ bands are shown. The solid line marked is the sum of the three bands to compare with the experimental data (open circles).

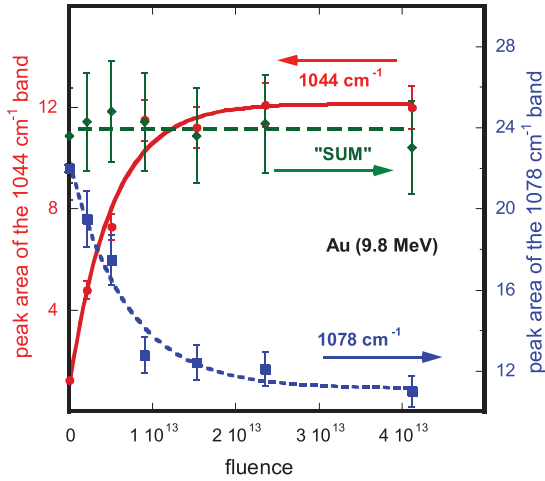


FIG. 3. (Color online) Structural transformation, areas of the 1044 (dotted line) and 1078 cm^{-1} (full line) bands as a function of ion fluence for Au at an energy of 9.8 MeV. The sum of the two areas is also plotted (dashed line), indicating that the decrease of the 1044- cm^{-1} band is compensated by the increase of the 1078- cm^{-1} band. The solid and dotted lines are fits of the data with Poisson's law.

of electronic energy loss and compared to previous track radii obtained from IR measurements for a beam energy of 5.3 MeV/amu,⁶ and by SAXS measurements³ for a Xe beam energy of 5 MeV/amu. The latter results also show that track radii derived from IR measurements are in agreement with those from SAXS analysis in the same regime of ion velocity. The second observation is that the radii measured at low velocity (0.2 MeV/amu) are larger than those measured at high velocity (5.3 MeV/amu) for the same electronic energy loss, as expected from the velocity effect.²⁹ In the case of Au irradiations, the radii are given in Table III. It can be seen that the radius obtained at the highest energy (14.8 MeV) is in agreement with the value from Kluth *et al.*,³ which was determined from SAXS results for irradiation with 22.7 MeV Au ions. The general dependence of the radii (or damage cross sections) on Au energy is surprising (Table III), since the radii determined in the nuclear collision dominant regime are of the same order of magnitude as those in the electronic

TABLE II. Radius deduced from the damage cross section for O, Si, and Ni ions. E_{av} is the average ion energy in the SiO_2 film. dE/dx_{ele} is the averaged electronic energy loss predicted by SRIM within the SiO_2 film.²² R_{exp} is the radius deduced from the experimental data and R_{model} is the radius calculated using the inelastic thermal spike model.

Ion	E_{av} (MeV)	dE/dx_{ele} (keV/nm)	R_{exp} (nm)	R_{model} (nm)
O	3.1	1.8	1.1 ± 0.2	0.8
Si	5.5	2.8	2.1 ± 0.3	2.0
Ni	11.4	4.2	2.9 ± 0.5	3.0

stopping dominant regime. Moreover, the radii exhibit a U shaped dependence on Au energy, where radii decrease from 4.9 ± 0.7 nm at 0.3 MeV to a minimum of 2.5 ± 0.4 / 2.6 ± 0.4 nm at 9.8/14.8 MeV, and then increase to 5.4 ± 0.1 nm at 168 MeV.³

III. DESCRIPTION OF TRACK EVOLUTION BY THERMAL SPIKE MODELS

A. The inelastic thermal spike model (i-TS)

The inelastic thermal spike model (i-TS) model^{26,27,29} was developed numerically to predict track radii in the electronic regime and applied to vitreous SiO_2 .^{3,9,18,34} It describes how the energy deposited on the electrons diffuses within the electron subsystem before it is transferred to the lattice atoms. The strength of the energy transfer is governed by the electron-phonon coupling. Such a model is able to describe quantitatively track formation in the electronic energy loss regime in various materials, including both metals²⁷ and insulators.²⁶ The model is described mathematically by two coupled differential equations in a cylindrical geometry governing the heat diffusion in time (t) and space (r) between the electronic and atomic subsystems:

$$C_e(T_e) \frac{\partial T_e}{\partial t} = \frac{1}{r} \frac{\partial}{\partial r} \left[r K_e(T_e) \frac{\partial T_e}{\partial r} \right] - g(T_e - T_a) + A(r[v], t), \quad (1)$$

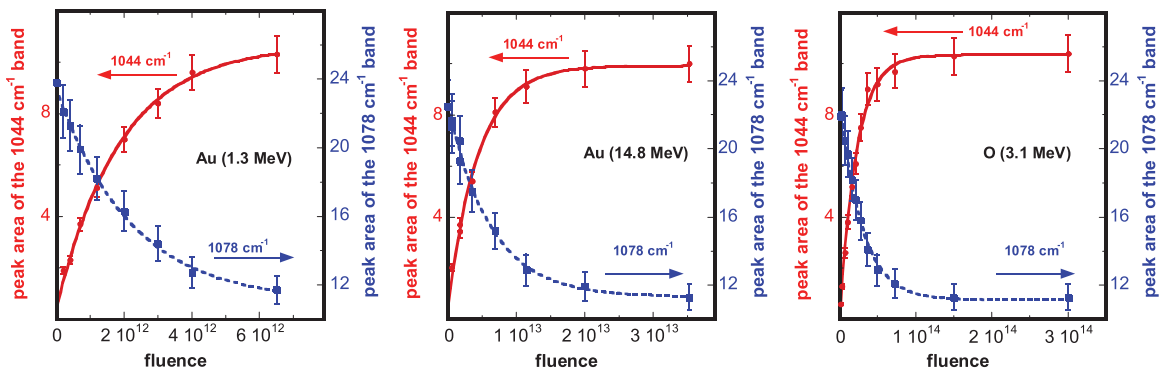


FIG. 4. (Color online) Structural transformation, areas of the 1044 (dotted line) and 1078 cm^{-1} (full line) bands as a function of ion fluence for Au ions with energies at 1.25 and 14.8 MeV and an O beam at 3.2 MeV. The results suggest that the decrease of the 1044- cm^{-1} band is compensated by the increase of the 1078- cm^{-1} band. The solid and dotted lines are fits of the data with Poisson's law.

TABLE III. Au ion-irradiation parameters and track radii (R_{exp}) determined from infrared spectroscopy. $dE/dx_{\text{ele}} - S$ is the averaged electronic stopping power predicted by SRIM within the SiO_2 film,²² $dE/dx_{\text{ele}} - R$ is the averaged electronic stopping power predicted by the reciprocity approach,²⁵ and dE/dx_{nuc} is the averaged nuclear stopping power predicted by SRIM in the SiO_2 film. R_{exp} is the mean track radius determined from the experimental cross section σ_{exp} given in Table I for energy up to 14.8 MeV, and the uncertainties in the experimental data were estimated to be $\sim 15\%$. The mean track radius determined from SAXS for higher energy above 27 MeV is also included.³ Model-predicted track radii, R_{model} , are given based on only electronic energy loss^{3,22} ($1-R_{\text{model}}$), based on total energy loss using SRIM-predicted electronic energy loss²² ($2-R_{\text{model}}$), and based on the total energy with reciprocity-predicted electronic energy loss²⁵ ($3-R_{\text{model}}$). The uncertainties in R_{model} are mainly attributed to the uncertainties in the total energy loss ($\sim 25\%$).

E_{av} (MeV)	$dE/dx_{\text{ele}}-S$ (keV/nm)	$dE/dx_{\text{ele}}-R$ (keV/nm)	dE/dx_{nuc} (keV/nm)	R_{exp} (nm)	$1-R_{\text{model}}$ (nm)	$2-R_{\text{model}}$ (nm)	$3-R_{\text{model}}$ (nm)
0.3	0.71	0.26	3.2	4.9 ± 0.7	0.2	4.4	4.4
0.6	1.11	0.37	3.1	4.7 ± 0.7	0.5	4.1	4.1
1.3	1.40	0.54	2.8	4.0 ± 0.6	0.9	4.0	3.7
2.3	1.70	0.71	2.3	3.0 ± 0.5	1.3	3.9	3.0
4.8	2.15	1.16	1.8	3.0 ± 0.5	1.5	3.6	2.7
9.8	2.57	2.14	1.2	2.5 ± 0.4	1.8	3.4	2.8
14.8	2.95	2.89	0.92	2.6 ± 0.4	2.1	3.3	3.0
27.4	4.0	—	0.70	2.4 ± 0.2	2.8	3.4	3.1
54	7.5	—	0.42	4.2 ± 0.1	4.3	4.3	4.3
89	11.0	—	0.29	4.9 ± 0.1	5.6	5.6	5.6
185	16.2	—	0.16	5.4 ± 0.1	6.4	6.4	6.4

$$C_a(T_a) \frac{\partial T_a}{\partial t} = \frac{1}{r} \frac{\partial}{\partial r} \left[r K_a(T_a) \frac{\partial T_a}{\partial r} \right] + g(T_e - T_a), \quad (2)$$

where $T_{e,a}$, $C_{e,a}$, and $K_{e,a}$ are temperature, specific heat, and thermal conductivity for the electronic and atomic structures, respectively. These two equations are solved numerically³⁵ to take into account the evolution of all the parameters versus $T_{e,a}$. The initial energy distribution on the electrons ($A(r[v],t)$), which depends on ion velocity (v), is deduced from Monte-Carlo calculations.³⁶ It is assumed that the deposited energy should be equal to the corresponding electronic energy loss when integrating, $A(r[v],t)$, over time and space. The electron-phonon coupling coefficient, g , is the only free parameter, and

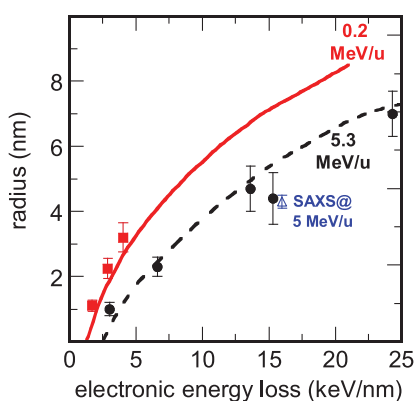


FIG. 5. (Color online) Track radii vs electronic energy loss²² for O, Si, and Ni irradiations at 0.2 MeV/amu compared to irradiation performed at ~ 5.3 MeV/amu.⁶ It should be noted that there is a good agreement within the experimental errors between the size of the tracks deduced from infrared measurements⁶ and SAXS measurements.³ The lines for the two quoted energies are the results of the radii calculations within the frame of the inelastic thermal spike model using an electron-phonon mean free path of $\lambda = 3$ nm.

is linked to the electron-phonon mean free path λ (Ref. 26) by the following relation: $\lambda = D_e C_e / g$, where D_e and K_e values are defined as constant values^{26,29} in the case of insulators. As described previously, the model calculations are performed within a superheating scenario,^{3,9,37} and the track radii are associated with the cylinder in which the energy deposited on the atoms surpasses the energy necessary to melt (E_m) the target material. This value of E_m , corresponding to the sum of the energy to reach the melting temperature plus the latent heat of fusion, is 0.38 eV/at for amorphous SiO_2 .

B. Applications of the i-TS model to low-Z ion irradiation

Applying this model to O ions used in the present experiment, the time evolution of the energy deposited on the atoms is shown in Fig. 6 using the electron-phonon mean free path of vitreous SiO_2 , $\lambda = 3$ nm, deduced from a fit of tracks measured by IR absorption at a beam energy of 5.3 MeV/amu.⁶ The deposited energy is larger than 0.38 eV/at for a radius smaller than 0.6 nm. Repeating the calculation for several values of electronic energy loss, the predicted radii as a function of S_e are plotted in Fig. 5 for beam energies of 0.2 and 5.3 MeV/amu. According to Waligorski *et al.*,³⁶ the initial energy density distribution on the electrons becomes larger when performing irradiations at 0.2 MeV/amu as compared to swift heavy ions (5.3 MeV/amu). Such evolution of the energy density on the electrons combined with the determined λ value for $a\text{-SiO}_2$ (Ref. 29) enables us to describe radii resulting from experiments performed at different beam energies,^{3,6,28,38,39} as well as for an Au beam larger than 0.10 MeV/amu.³ However, the extrapolation of this model³ fails completely for Au beam energies less than 0.05 MeV/amu (~ 10 MeV of Au), where electronic energy loss becomes comparable to nuclear energy loss. Moreover, the observed evolution of the damage cross sections cannot be explained by the nuclear collision cross section determined

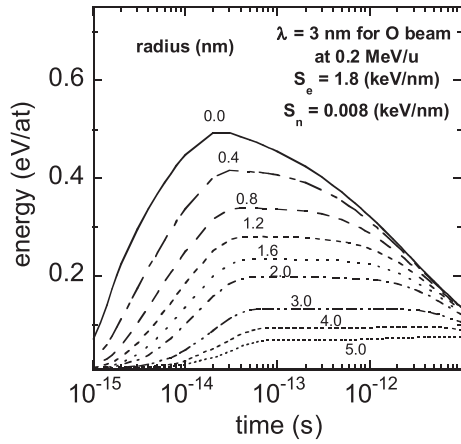


FIG. 6. Energy deposited on the atoms vs time for an irradiation with O ions at 0.2 MeV/amu calculated with the inelastic thermal spike model ($S_e = -dE/dx_{ele}$ and $S_n = -dE/dx_{nucl}$).

by SRIM.^{22,40} For example, for Au irradiation at 15 MeV, the number of displacements in SiO₂ is 5.5 per nm per ion, assuming displacement energies of 28 and 15 eV for O and Si, respectively. Such a number divided by the number of atoms per cm³ gives a damage cross section of 8×10^{-16} cm² (Table I) that is at least two orders of magnitude lower than the measured value. These facts suggest that a combination of the elastic collision spike model³⁰ and the inelastic thermal spike model²⁶ is necessary to describe the observed U-shaped dependence.

C. The unified thermal spike model

To develop a unified model, an additional contribution resulting from nuclear energy deposition³⁰ contributing to a molten zone⁴¹ is added to Eq. (2), describing the energy input into the atomic system. In analogy to the electronic energy density, the nuclear energy density is written as $B(r,t) = b_n \times S_n \times e^{-t/\tau} \times e^{-r/r_0}/r$, where τ is the deposition time and r_0 is the radius of a cylinder in which the nuclear energy is deposited. The constant b_n was chosen so that integration over time and space yields the total nuclear energy loss S_n (Table I). To determine r_0 , the mean energy transfer $\langle T \rangle$ to

Si and O atoms was calculated from the screened elastic scattering cross section^{42,43} and is shown as a function of Au ion energy in Fig. 7(a). Using SRIM,²² the corresponding mean range is calculated and plotted versus beam energy in Fig. 7(b). Within a first-order approximation, the calculated ranges of O and Si in *a*-SiO₂ are similar, and a mean range value is determined and shown in Fig. 7(c). Due to the kinematics of ion-ion collisions, low-energy atoms are emitted perpendicular to the ion trajectory, leading to a mean spike radius, r_0 , of 7.3, 9.6, and 8.5 nm for Au ions at 0.3, 2.3, and 14.8 MeV, respectively. Likewise, by assuming that the nuclear energy loss is deposited within r_0 , the mean deposited energy on the atoms is given in Fig. 7(c). The effect of variation in time and space for the energy deposition has been tested for the determination of the radius: a variation of the deposition time by a factor of 4 (between 5×10^{-14} and 2×10^{-13} s) causes only a 10% difference in the molten radius, while a 50% increase of r_0 leads to a 50% variation in the molten radius.

Applying the calculation to the case of 0.6 MeV Au, the evolution of the energy deposited on the atoms is shown as a function of time in Fig. 8, where the nuclear energy loss is nearly 80% of the total energy loss to the atoms (Table I). It is observed that the energy deposited to the atoms by electronic energy loss [Fig. 8(a)] is at least a factor of 10 smaller than that deposited by the nuclear energy loss [Fig. 8(b)]. Combining nuclear and electronic energy losses, the evolution of the energy density on the atoms is plotted versus time [Fig. 8(c)]. Using the melting criteria, a cylinder radius of 4.1 nm is derived from the results in Fig. 8(c), in agreement with the present measurement within the experimental errors (Table III).

The results of the radii calculations as a function of Au beam energy are shown in Fig. 9 for all three models: nuclear energy loss only by the elastic collisions spike model,³⁰ electronic energy loss only by the inelastic thermal spike model, and total energy loss by the unified thermal spike model. For the electronic energy loss, SRIM²² predicted stopping values are used. As indicated in Fig. 9, it is possible to describe the U-shaped dependence of the radii on Au ion energies. There is a very good agreement at low energies (Au energy less than 1.5 MeV) and at very high energies (Au energy larger than 20 MeV). However, the unified thermal spike model predicts higher values of radii in the intermediate regime as compared to experiment. Such calculations are extrapolated to

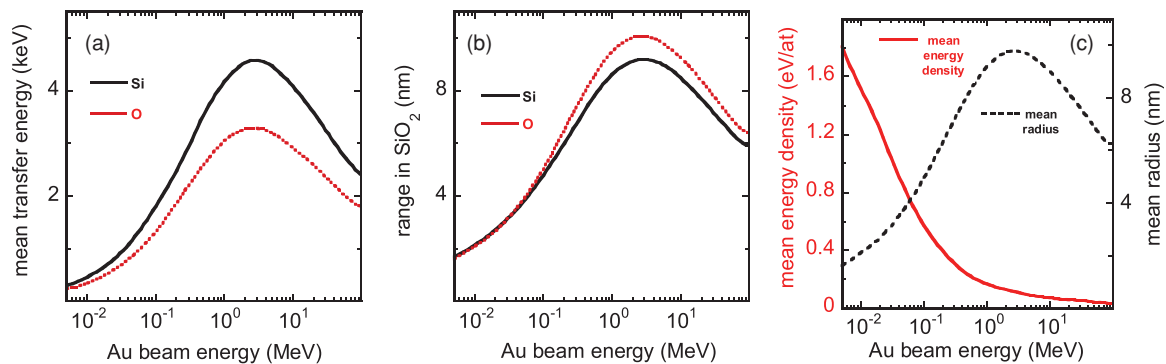


FIG. 7. (Color online) Mean energy transfers to Si and O atoms vs Au beam energy (a) and the corresponding range of Si and O atoms in vitreous SiO₂ (b). Mean value of ion range and mean energy deposited on the atoms are plotted vs Au beam energy in (c).

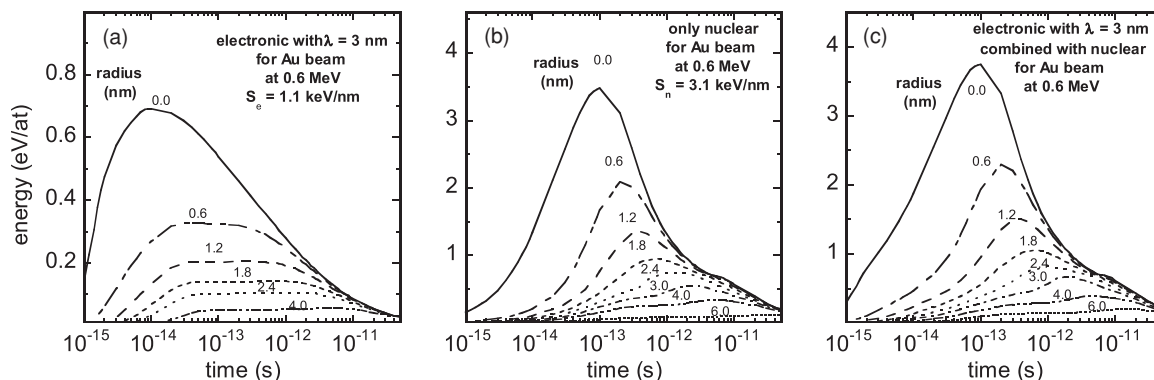


FIG. 8. Evolution of the energy on the atoms vs time in the case of an Au ion at 0.6 MeV beam energy based on (a) pure electronic energy loss ($S_e = -dE/dx_{ele}$) using SRIM,²² (b) pure nuclear energy loss ($S_n = -dE/dx_{nucl}$), and (c) a combination of the two processes of energy losses (dE/dx_{total}).

an Au beam energy of 5 keV, showing that the molten radius decreases for energies lower than 100 keV despite the increase in mean deposited energy density [Fig. 7(c)]. This is the result of the very high cooling rate, which hinders the diffusion of the energy on the lattice atoms;⁴⁴ the cooling rate increases when r_0 decreases since the surface-to-volume ratio of a cylinder follows $1/r_0$.

D. Determination of the electronic energy loss

The SRIM code is widely used for calculating stopping powers in matter. Since the stopping prediction from SRIM is based on fits to experimental data, it usually provides reasonable predictions. However, recent studies have also shown a large

overestimation of the electronic stopping power by a factor of 2 for Au ions in targets containing light elements⁴⁵⁻⁴⁷ such as in SiC,⁴⁶ GaN,⁴⁷ and SrTiO₃.⁴⁵ Sigmund²⁵ has suggested that the electronic stopping cross section may be determined from the inverted ion-target system by applying the concept of reciprocity. The principle of reciprocity is based on the invariance of the inelastic excitation in ion-atom collisions against interchange of projectile and target, and is applicable in the low-velocity regime ($E \leq 25$ keV/amu), where the projectiles are neutral and the probability for electron loss is small. Better agreements between the reciprocity prediction and experimental stopping results have been reported.⁴⁵⁻⁴⁷ The electronic stopping cross sections for Si and O ions in Au can be obtained from SRIM in units of 10^{-15} eV atoms⁻¹ cm², and by applying the reciprocity principle,²⁵ these values are used as electronic stopping cross sections for Au ions in Si and O, respectively. By further applying Bragg's rule, the total stopping cross section for Au ions in SiO₂ can be derived.

Specific calculations have been performed for 4.8 and 9.8 MeV Au ion energies and are shown in Fig. 10. Included in Fig. 10 are the calculations for energy deposited on the atoms with only electronic energy loss using the corrected values resulting from the reciprocity approach²⁵ [Figs. 10(a) and 10(d)], with only the nuclear energy loss²² [Figs. 10(b) and 10(e)], and with the total energy loss from nuclear and electronic losses [Figs. 10(c) and 10(f)]. Although the energy deposition on the atoms differs significantly between Figs. 10(a) and 10(d) (only the electronic energy loss) and between Figs. 10(b) and 10(e) (only the nuclear energy loss), the results in Figs. 10(c) and 10(f) are similar, confirming that the decrease of the nuclear energy loss from 4.8 and 9.8 MeV Au beams is compensated by the increase of electronic energy loss. Applying the molten criteria to the results in Figs. 10(c) and 10(f), track radii of 2.7 and 2.8 nm are derived for the two energies, in much better agreement with experimental values (Table III). The results of the calculated radii using a combination of the nuclear energy loss predicted by SRIM²² with the electronic energy loss predicted using the reciprocity approach²⁵ for Au energy less than 20 MeV are shown in Fig. 11. The results in Fig. 11 are complemented by the results of the i-TS model for Au beam energies larger than 20 MeV using SRIM values.^{3,22} The U shape of the radius

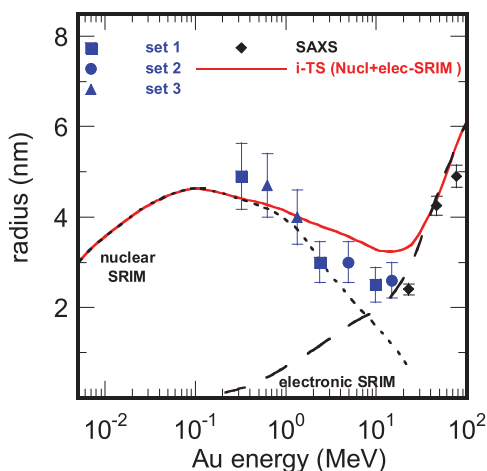


FIG. 9. (Color online) Track radii vs Au beam energy. Three sets of irradiations were carried out with Au energies at 0.3, 2.3, and 9.8 MeV for the first run (set 1), 4.8 and 14.8 MeV for the second run (set 2), and 0.6 and 1.3 MeV for the third run (set 3). For comparison, also included are track radii deduced from SAXS measurements (diamonds), the calculated radius of the molten phase using the elastic collision spike model resulting from the nuclear energy loss (SRIM) (short dashed line), results from previous i-TS calculations for Au ions³ with electronic energy loss deduced from SRIM and an electron phonon mean free path $\lambda = 3$ nm (dashed line), as well as the results from the unified spike model (present calculations) with the electronic energy loss estimated by SRIM²² (solid line).

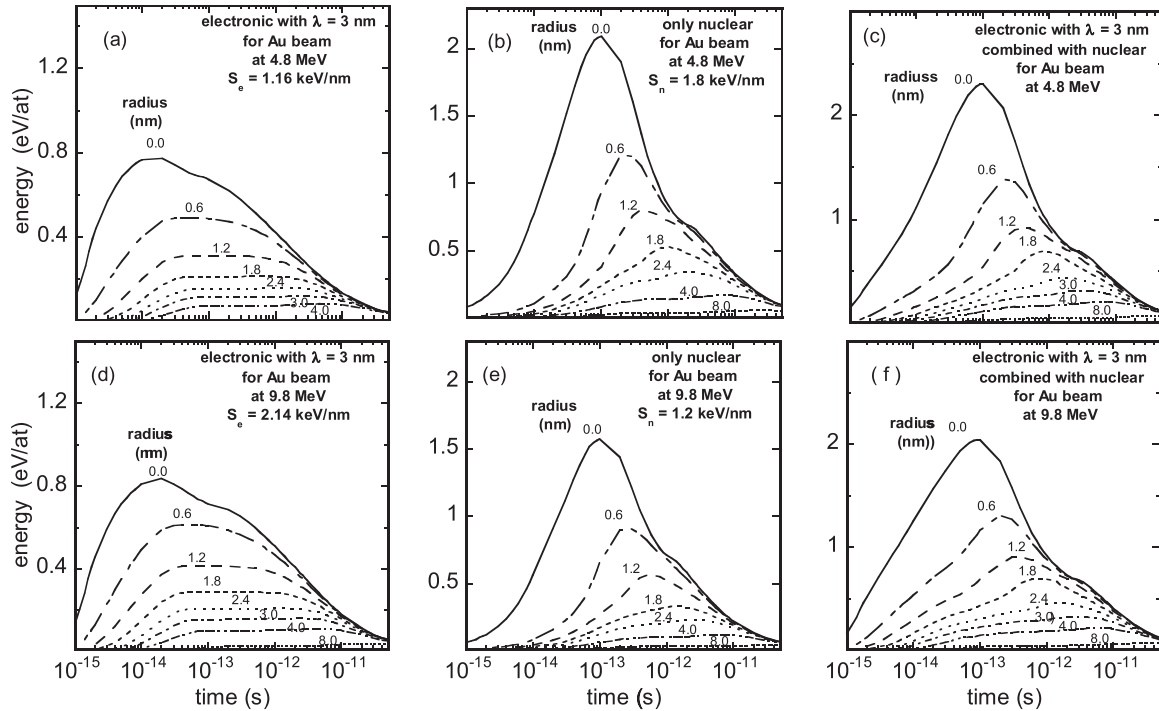


FIG. 10. Evolution of the energy on the atoms vs time in the case of an Au ion at 4.8 and 9.8 MeV beam energy. (a,d) Pure electronic energy loss using Sigmund theory,²⁵ (b,e) pure nuclear energy loss (SRIM²²), (c,f) a combination of the two processes of energy losses ($S_e = -dE/dx_{ele}$ and $S_n = -dE/dx_{nucl}$).

evolution is well predicted as a function of Au beam energy in the intermediate regime, confirming the synergy between the two energy loss regimes in the energy range between 2 and 15 MeV. Such good agreement suggests that SRIM overestimates the electronic energy loss at low energy for high-Z ions impinging materials composed of low-Z atoms, as experimentally shown previously.⁴⁵⁻⁴⁷ Moreover, it is predicted that large structural modifications can appear even at very low beam energies.

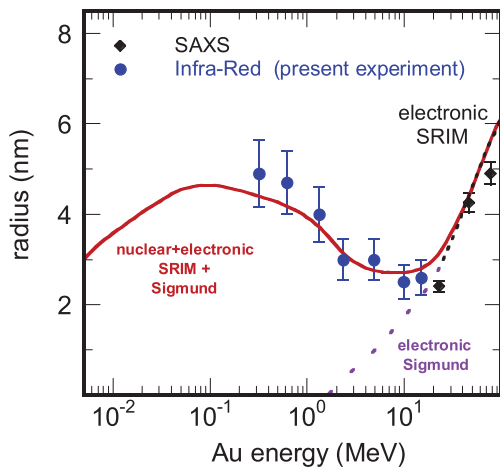


FIG. 11. (Color online) Radii calculations using only the electronic energy losses (reciprocity²⁵ for beam energy less than 20 MeV and SRIM²² for higher energy) (dotted line) and a combination of nuclear and electronic energy losses (solid line).

IV. CONCLUSIONS

In conclusion, structural modification of vitreous SiO₂ by Au ion irradiation in the energy range between 0.3 and 15 MeV was measured using infrared spectroscopy. By analyzing the evolution of the peak area of the infrared bands versus ion fluence, the track radii evolve from 4.9 nm for an Au beam energy at 0.3 MeV to a minimum value of about 2.5 nm between 9.8 and 14.8 MeV. Combined with the results of Kluth *et al.*,³ track radii exhibit a U-shaped dependence on Au ion energies, as the track radius increases from 2.4 nm at 23 MeV to 5.4 nm at 168 MeV. Using the unified thermal spike model, a combination of the elastic collision spike model and the inelastic thermal spike model based on electronic energy losses derived from the reciprocity approach, it is possible to fully describe the experimental data, which clearly demonstrate a synergy between the nuclear energy loss and the electronic energy loss processes. Large damage cross sections for Au ion energy less than 1 MeV reachable by low-energy heavy recoil nuclei (α recoils) through α decay of actinide elements indicate a very localized but significant damage process. This may have major implications in material applications, such as for immobilization of nuclear waste.

ACKNOWLEDGMENTS

Research supported by the US Department of Energy, Basic Energy Sciences, Materials Sciences and Engineering Division. A portion of research was performed at the Environmental Molecular Sciences Laboratory (EMSL), a national scientific user facility sponsored by the Department

of Energy's Office of Biological and Environmental Research and located at Pacific Northwest National Laboratory.

P.K. acknowledges the Australian Research Council for support.

*Author to whom all correspondence should be addressed: Zhangy1@ornl.gov

- ¹W. J. Weber, R.C. Ewing, C.R.A. Catlow, T. D. de la Rubia, L. W. Hobbs, C. Kinoshita, H. Matzke, A. T. Motta, M. Nastasi, E. K. H. Salje, E. R. Vance and S. J. Zinkle, *J. Mater. Res.* **13**, 1434 (1998).
- ²W. J. Weber, A. Navrotsky, S. Stefanovsky, E. R. Vance, and E. Vernaz, *MRS Bull.* **34**, 46 (2009).
- ³P. Kluth, C. S. Schnohr, O. H. Pakarinen, F. Djurabekova, D. J. Sprouster, R. Giulian, M. C. Ridgway, A. P. Byrne, C. Trautmann, D. J. Cookson, K. Nordlund, and M. Toulemonde *Phys. Rev. Lett.* **101**, 175503 (2008).
- ⁴A. Benyagoub, S. Löffler, M. Rammensee, S. Klaumünzer, and G. Saemann-Ischenko, *Nucl. Instrum. Methods* **65**, 228 (1992).
- ⁵M. C. Busch, A. Slaoui, P. Siffert, E. Dooryhee, and M. Toulemonde, *J. Appl. Phys.* **71**, 2596 (1992).
- ⁶C. Rotaru, Ph.D. thesis, University of Caen (2004); [<http://tel.archives-ouvertes.fr/tel-00005399/fr/>].
- ⁷K. Awazu, S. Ishii, K. Shima, S. Roorda, and J. L. Brebner, *Phys. Rev. B* **62**, 3689 (2000).
- ⁸M. Toulemonde, C. Trautmann, E. Balanzat, K. Hjort, and A. Weidinger, *Nucl. Instrum. Methods Phys. Res. B* **216**, 1 (2004).
- ⁹A. Dallanora, T. L. Marcondes, G. G. Bermudez, P. F. P. Fichtner, C. Trautmann, M. Toulemonde, and R. M. Papaléo, *J. Appl. Phys.* **104**, 024307 (2008).
- ¹⁰B. Canut, M. G. Blanchin, S. Ramos-Canut, V. Teodorescu, and M. Toulemonde, *Nucl. Instrum. Methods Phys. Res. B* **245**, 327 (2006).
- ¹¹M. Toulemonde, S. M. M. Ramos, H. Bernas, C. Clerc, B. Canut, J. Chaumont, and C. Trautmann, *Nucl. Instrum. Methods Phys. Res. B* **178**, 331 (2001).
- ¹²R. A. B. Devine, *Nucl. Instrum. Methods Phys. Res. B* **91**, 378 (1994).
- ¹³P. Mazzoldi, P. Mazzoldi, A. Carnera, F. Caccavale, M. L. Favaro, A. Boscolo-Boscoletto, G. Granozzi, R. Bertinello, and G. Battaglin, *J. Appl. Phys.* **70**, 3528 (1991).
- ¹⁴B. Garrido, J. Samitier, J. R. Morante, J. Montserrat, and C. Dominguez, *Phys. Rev. B* **49**, 14845 (1994).
- ¹⁵E. P. EerNisse and C. B. Norris, *J. Appl. Phys.* **45**, 5196 (1974).
- ¹⁶C. M. Johnson, M. C. Ridgway, and P. W. Leech, *Appl. Phys. Lett.* **69**, 984 (1996).
- ¹⁷E. Snoeks, A. Polman, and C. A. Volkert, *Appl. Phys. Lett.* **65**, 2487 (1994).
- ¹⁸A. Benyagoub, S. Klaumünzer, and M. Toulemonde, *Nucl. Instrum. Methods Phys. Res. B* **146**, 454 (1998).
- ¹⁹T. van Dillen, A. Polman, W. Fukarek, and A. v. Blaaderen, *Appl. Phys. Lett.* **78**, 910 (2001).
- ²⁰T. van Dillen, A. Polman, C. M. v. Kats, and A. v. Blaaderen, *Appl. Phys. Lett.* **83**, 415 (2003).
- ²¹A. Meftah, F. Brisard, J. M. Costantini, M. Hage-Ali, J. P. Stoquert, F. Studer, and M. Toulemonde, *Phys. Rev. B* **48**, 920 (1993).
- ²²J. F. Ziegler, J. P. Biersack, and M. D. Ziegler, *The Stopping and Range of Ions in Solids* (SRIM Co., 2008).
- ²³J. Jensen, A. Razpet, M. Skupinski, and G. Possnert, *Nucl. Instrum. Methods Phys. Res. B* **243**, 119 (2006).
- ²⁴J. Jensen, A. Razpet, M. Skupinski, and G. Possnert, *Nucl. Instrum. Methods Phys. Res. B* **245**, 269 (2006).
- ²⁵P. Sigmund, *Eur. Phys. J. D* **47**, 45 (2008).
- ²⁶A. Meftah, J. M. Costantini, N. Khalfaoui, S. Boudjadar, J. P. Stoquert, F. Studer, and M. Toulemonde, *Nucl. Instrum. Methods Phys. Res. B* **237**, 563 (2005).
- ²⁷Z. G. Wang, C. Dufour, E. Paumier, and M. Toulemonde, *J. Phys.: Condens Matter* **6**, 6733 (1994); **7**, 2525(E) (1994).
- ²⁸J. Mangano, J. Olivares, F. Agullo-Lopez, M. L. Crespillo, A. Morono, and E. Hodgson, *Nucl. Instrum. Methods B* **268**, 3147 (2010).
- ²⁹M. Toulemonde, W. Assmann, C. Dufour, A. Meftah, F. Studer, and C. Trautmann, *Mat. Fys. Medd.* **52**, 263 (2006).
- ³⁰P. Sigmund and C. Claussen, *J. Appl. Phys.* **52**, 990 (1981).
- ³¹H. D. Mieskes, W. Assmann, F. Grüner, H. Kucal, Z. G. Wang, and M. Toulemonde, *Phys. Rev. B* **67**, 155404 (2003).
- ³²M. Toulemonde, *Nucl. Instrum. Methods Phys. Res. B* **250**, 263 (2006).
- ³³P. Thévenard, G. Guiraud, C. H. S. Dupuy, and B. Delaunay, *Rad. Eff.* **32**, 83 (1977).
- ³⁴M. Toulemonde, C. Dufour, E. Paumier, and F. Pawlak, *MRS Proc.* **504**, 99 (1988).
- ³⁵M. Toulemonde, C. Dufour, A. Meftah, and E. Paumier, *Nucl. Instrum. Methods Phys. Res. B* **166-167**, 903 (2000).
- ³⁶M. P. R. Waligorski, R. N. Hann, and R. Katz, *Nucl. Tracks Rad. Meas.* **11**, 309 (1986).
- ³⁷M. Toulemonde, W. Assmann, C. Trautmann, and F. Grüner, *Phys. Rev. Lett.* **88**, 057602 (2002).
- ³⁸T. Mohanty, N. C. Mishra, S. V. Bhat, P. K. Basu, and D. Kanjilal, *J. Phys. D* **36**, 3151 (2003).
- ³⁹T. Mohanty, P. V. Satyam, N. C. Mishra, and D. Kanjilal, *Rad. Meas.* **36**, 137 (2003).
- ⁴⁰J. P. Biersack and L. G. Haggmark, *Nucl. Instrum. Methods* **174**, 257 (1980).
- ⁴¹K. Nordlund, J. Peltola, J. Nord, J. Keinone, and R. S. Averback, *J. Appl. Phys.* **90**, 1710 (2001).
- ⁴²J. Lindhard, V. Nielsen, M. Scharf, and K. D. Videnskab, *Mat.-Fys. Medd.* **36**, No. (1968).
- ⁴³E. Balanzat and S. Bouffard, *Solid State Phenom.* **30-31**, 7 (1993).
- ⁴⁴J. Zhang, M. Lang, R. C. Ewing, R. Devanathan, W. J. Weber, and M. Toulemonde, *J. Mater. Res.* **25**, 1345 (2010).
- ⁴⁵Y. Zhang, J. Lian, Z. Zhu, W. D. Bennett, L. V. Saraf, J. L. Rausch, C. A. Hendricks, R. C. Ewing, and W. J. Weber, *J. Nucl. Mater.* **389**, 303 (2009).
- ⁴⁶Y. Zhang, I.-T. Bae, K. Sun, C. Wang, M. Ishimaru, Z. Zhu, W. Jiang, and W. J. Weber, *J. Appl. Phys.* **105**, 104901 (2009).
- ⁴⁷Y. Zhang, M. Ishimaru, J. Jagielski, W. Zhang, Z. Zhu, L. V. Saraf, W. Jiang, L. Thomé, and W. J. Weber, *J. Phys. D* **43**, 085303 (2010).